Article

CoFe$_2$O$_4$ Nanoparticles Grown within Porous Al$_2$O$_3$ and Immobilized on Graphene Nanosheets: A Hierarchical Nanocomposite for Broadband Microwave Absorption

Debika Gogoi, Raghavendra Korde, Virendra Singh Chauhan, Manoj Kumar Patra, Debmalya Roy, Manash R. Das, and Narendra Nath Ghosh*

Cite This: ACS Omega 2022, 7, 28624−28635

Read Online

ACCESS | Metrics & More | Article Recommendations | SI Supporting Information

ABSTRACT: Demands to develop efficient microwave-absorbing materials are increasing with the advancement of information technology and the exponential rise in the usage of electromagnetic devices. To reduce electromagnetic interference and to overcome the adverse effects caused by microwave exposure resulting from the excessive usage of electromagnetic devices, microwave absorbers are very necessary. In addition, radar-absorbing materials are essential for stealth technology in military applications. Herein, we report a nanocomposite in which CoFe$_2$O$_4$ (CF) nanoparticles were grown within the porous structure of Al$_2$O$_3$ (PA), and this CoFe$_2$O$_4$-loaded Al$_2$O$_3$ (PA−CF) nanocomposite was immobilized on the surface of nanometer-thin graphene sheets (Gr). Owing to the hierarchical structure created by the constituents, the (60PA-40CF)$_{90}$-Gr$_{10}$ nanocomposite exhibited excellent microwave-absorption properties in the X-band region with a reflection loss (RL) value of ∼−30.68 dB (∼99.9% absorption) at 10.71 and 9.04 GHz when thicknesses were 2.0 and 2.3 mm, respectively. This nanocomposite demonstrated its competence as a lightweight, high-performance microwave absorber in the X-band region, which can be utilized in the applications of pioneering stealth technology.
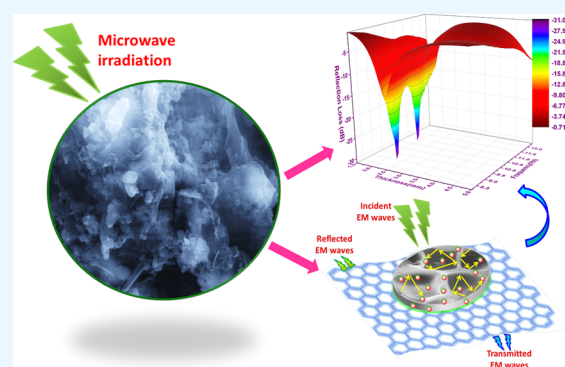
1. INTRODUCTION

In this modern era of technology, electromagnetic (EM) devices have become an integral part of our day-to-day lives. The exponential augmentation of information technology (IT) and extensive use of electronic and electrical devices, wireless communications, local area networks, radar systems, etc. cause electromagnetic interference (EMI).[1−3] In addition, the EM radiations generated by these devices create EM pollution globally and pose some adverse effects on human health as well as on other biological systems.[4−6] The high-frequency microwave (MW) induces some undesirable EM noise, which not only interrupts the electronically controlled systems but also harms human health by elevating the temperature in living tissues and weakening the immune system of the body.[7] Moreover, overexposure to MW may also enhance the risk of cancer, tachycardia, induces damage to DNA strands in the rat brain cells, etc.[4,8] These reasons are triggering the demand to develop MW-absorbing materials. These materials have imminent applications in various fields such as EMI shielding, information security, healthcare, military applications like stealth technology, etc.[4,9] Radar-absorbing materials (RAMs) are particularly used in the defense sector, which can efficiently absorb MW in the X-band region (8.2−12.4 GHz).[4,10] The advanced radar stealth appliances demand new and high-performance RAMs with advanced properties, such as low density, thin-layered structures, lightweight, strong absorption, broad effective bandwidth, high-temperature stability, etc.[4,11−13]

To conform to the requirements of the high-performance radar-absorbing materials, we have designed nanocomposites where CoFe$_2$O$_4$ (CF) nanoparticle-loaded porous Al$_2$O$_3$ (PA) particles (PA−CF) are immobilized on the surface of nanometer-thin graphene (Gr) sheets. During the designing of these nanocomposites, the following criteria were considered: (i) Al$_2$O$_3$ possesses dielectric property[14,15] and (ii) the porous structure of PA can provide plentiful solid−air interfaces, which can enhance the interfacial polarization during interaction with MW and also can increase the propagation pathway of MW. Moreover, the presence of PA makes the nanocomposite structure simultaneously lightweight, mechanically robust, and high-temperature corrosion resistance.[16] (iii) Owing to the magnetic nature of CF

Scheme 1. Schematic Representation of the Synthesis of PA, PA−CF, and ((PA−CF)$_x$−Gr)$_y$ Nanocomposites
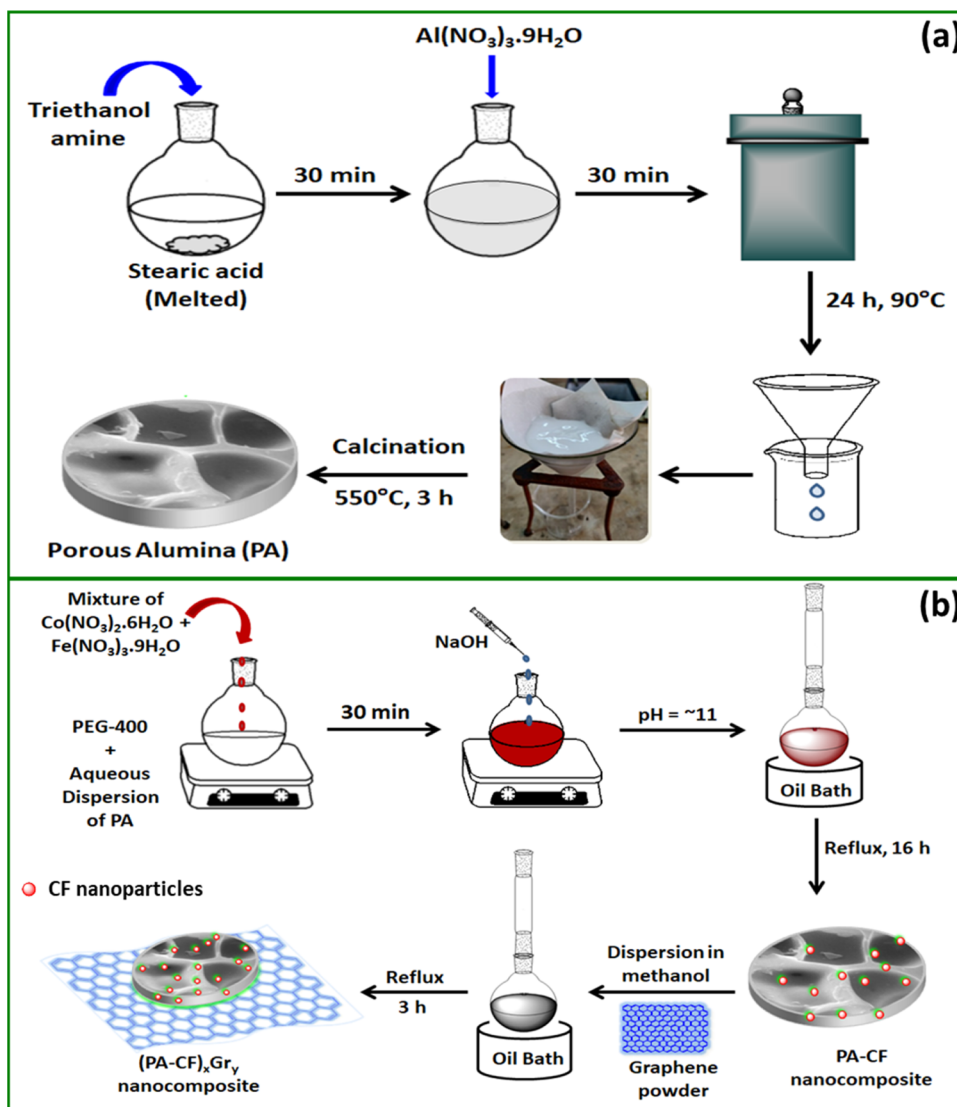
nanoparticles, their presence can generate magnetic loss characteristics via a natural resonance mechanism and can enhance the MW-absorption property of the nanocomposite.[4,17−21] (iv) As PA (a dielectric material) is in close contact with CF (a magnetic material), more polarization charges generate on the surface of PA, which enhances the dielectric loss effect.[14] (v) In this composite, the presence of graphene is also beneficial because it can provide necessary electrical conductivity and a high surface area where PA−CF particles are immobilized, which is helpful not only to weaken the effects of the EM waves by transferring them into thermal energy but also to keep the structural stability.[18,22,23]

Herein, we report the synthesis of a nanocomposite composed of CF, PA, and Gr. First, porous PA was synthesized and then CF nanoparticles were grown within the pores and surface of PA. After the preparation of PA−CF, their microwave-absorption property was determined. Since it was observed that the nanocomposite having 60 wt % PA and 40 wt % CF (60PA-40CF) manifested the best microwave-absorption property [in terms of reflection loss (RL)], we further synthesized nanocomposites composed of 60PA-40CF and graphene. It was observed that the nanocomposite (60PA-

40CF)90-Gr10 exhibited the highest RL value of ∼−30.68 dB (∼99.9% absorption) at 10.71 and 9.04 GHz when the thicknesses were 2.0 and 2.3 mm, respectively.

2. EXPERIMENTAL SECTION

2.1. Synthesis of Porous Al$_2$O$_3$−CoFe$_2$O$_4$−Graphene Nanocomposites ((PA−CF)$_x$−Gr$_y$). The synthesis of ((PA−CF)$_x$−Gr$_y$) nanocomposites was carried out using the following three-step methodology:

Step I: Porous Al$_2$O$_3$ (PA) was synthesized by employing an aqueous solution-based procedure, which was previously reported by us.[24] A gel was prepared from a reaction mixture of Al(NO$_3$)$_3$·9H$_2$O, triethanolamine, and stearic acid. This gel was then hydrothermally treated at 90 °C for 24 h, followed by calcination at 550 °C for 3 h to obtain PA.

Step II: To grow CoFe$_2$O$_4$ (CF) nanoparticles within the pores of PA support, a mixture of Co(NO$_3$)$_2$·6H$_2$O and Fe(NO$_3$)$_3$·9H$_2$O in poly(ethylene glycol) (PEG) was added in a dispersion of PA in H$_2$O. In this mixture, a 2 M NaOH aqueous solution was added dropwise till pH ∼ 11. Then, the temperature was increased to 160 °C and refluxed for 16 h. The precipitate formed was then washed with H$_2$O and dried.
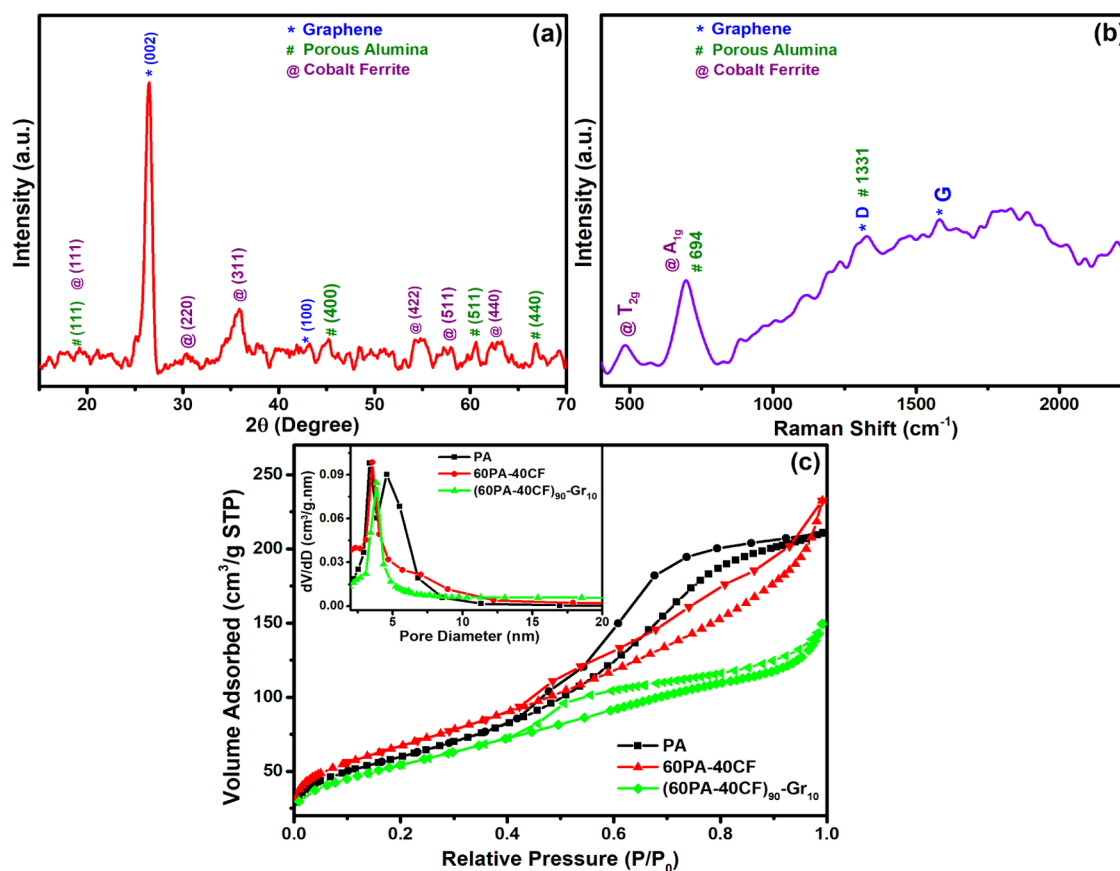
Figure 1. (a) XRD pattern $(60PA-40CF)_{90}-Gr_{10}$; (b) Raman spectrum of $(60PA-40CF)_{90}-Gr_{10}$; and (c) N_2 adsorption−desorption isotherms of PA, 60PA-40CF, and $(60PA-40CF)_{90}-Gr_{10}$; the inset displays the pore size distribution plots of PA, 60PA-40CF, and $(60PA-40CF)_{90}-Gr_{10}$.

By employing this protocol, samples were prepared having various amounts of PA and CF (such as 90PA-10CF, 80PA-20CF, 70PA-30CF, 60PA-40CF, 50PA-50CF where the weight % of PA was 90, 80, 70, 60, and 50%, respectively). Pure CF nanoparticles were also prepared using this method, without the addition of PA.[25]

Step III: A simple wet impregnation technique was used to decorate the surface of graphene sheets with the 60PA-40CF nanocomposite. Calculated amounts of graphene (Gr) and 60PA-40CF were dispersed in methanol and then refluxed at 70 °C for 4 h. The obtained black-colored solid powder was then filtered and dried. Nanocomposites with varying amounts of Gr and 60PA-40CF were prepared, where the Gr content was varied from 10 to 90 wt % (e.g., $(60PA-40CF)_{90}-Gr_{10}$, $(60PA-40CF)_{75}-Gr_{25}$, $(60PA-40CF)_{50}-Gr_{50}$, $(60PA-40CF)_{25}-Gr_{75}$, $(60PA-40CF)_{10}-Gr_{90}$). The schematic presentation of the synthesis methodology has been illustrated in Scheme 1. The detailed synthetic protocols and characterizations are provided in the Supporting Information.

2.2. Microwave-Absorption Measurement. To determine the microwave-absorption property of the as-synthesized materials, measurements were conducted in the X-band (8.2−12.4 GHz) range by measuring complex permeability and complex permittivity using an HP 8510 vector network analyzer. Details of the sample preparation for MW-absorption measurements are provided in the Supporting Information.

3. RESULTS AND DISCUSSION

3.1. Crystal Structure, Morphology, and Formation of the Synthesized Materials. The crystalline phases of the synthesized materials were identified using X-ray diffraction (XRD) analysis. The XRD pattern of PA displayed diffraction peaks at 2θ = 19.2, 36.8, 45.7, 60.3, and 66.4°, which correspond to the (111), (311), (400), (511), and (440) crystal planes of γ-Al_2O_3 [JCPDS Card no: 10-0425] (Figure S1a).[26] Pure CF showed XRD peaks at 2θ = 18.4, 30.3, 35.6, 37.4, 43.3, 53.7, 57.2, and 62.7°, which arises due to the presence of the (111), (220), (311), (222), (400), (422), (511), and (440) crystallographic planes of CF with a cubic crystal system [JCPDS Card no: 22-1086] (Figure S1b).[27] In the case of pure graphene (Gr), the diffraction peaks appeared at 2θ = 25.4 and 43.3°, which correspond to the (002) and (100) planes of graphene [JCPDS Card no: 01-0646] (Figure S1d). The XRD patterns of PA−CF nanocomposites display all of the characteristic peaks of both PA and CF and as a representative, the XRD pattern of 60PA-40CF is displayed in Figure S1c. In the XRD pattern of the nanocomposite $(60PA-40CF)_{90}-Gr_{10}$, the peaks were observed at 2θ = 19.2, 26.2, 30.4, 35.9, 43.2, 45.5, 57.1, 62.9, and 66.9°, which confirm the presence of PA, CF, and Gr in the final nanocomposite (Figure 1a), and the XRD patterns of other compositions are presented in Figure S2.

Figure S3a shows the Raman spectra of pure graphene, in which the presence of sharp peaks at 1323, 1578, and 2732 cm^{-1} corresponding to D, G, and 2D bands of graphene, respectively, were observed.[28] The number of layers was calculated using the peak position of G and the equation (eq 1), as shown below.
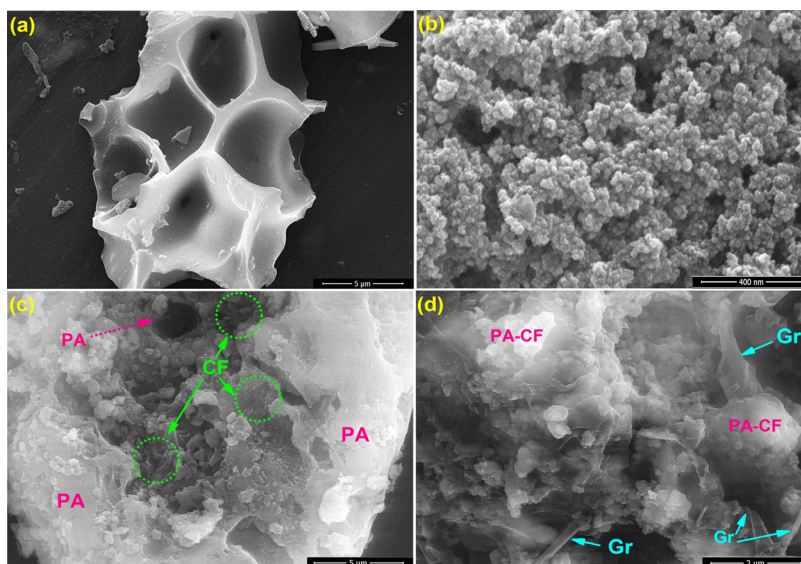
Figure 2. FESEM micrographs of (a) PA, (b) CF, (c) 60PA-40CF, and (d) $(60PA\text{-}40CF)_{90}\text{-}Gr_{10}$.
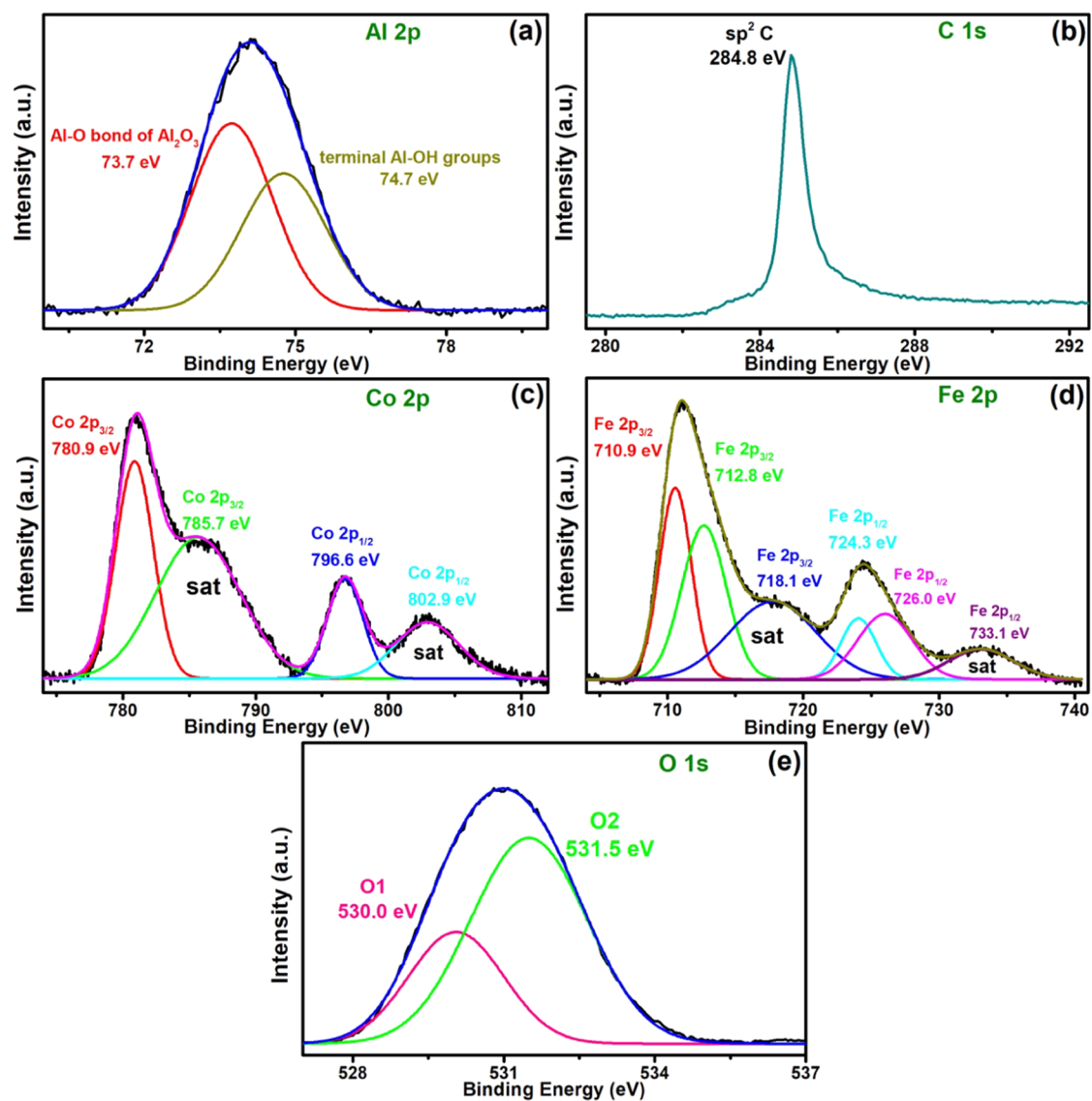

Figure 3. High-resolution XPS spectra of (a) Al 2p, (b) C 1s, (c) Co 2p, (d) Fe 2p, and (e) O 1s for the $(60PA\text{-}40CF)_{90}\text{-}Gr_{10}$ nanocomposite.

$$\omega_G = 1581.6 + \frac{11}{1 + n^{1.6}} \qquad (1)$$

where ω_G is the band position in the wavenumber and n is the number of layers present in the sample.[29] It was found that the number of layers of this Gr sample is ~1.2. The single and sharp 2D peak indicated the almost single-layer nature of this Gr. The Raman spectrum of CF (Figure S3b) displayed peaks at 456 cm^{-1} (T_{2g} vibrational mode of octahedral iron), 589 cm^{-1} (vibrational mode of an oxygen anion at tetrahedral sites (MO_4)), and 662 cm^{-1} (A_{1g} vibrational mode of tetrahedral cobalt).[30,31] In the case of PA, the absence of any distinct peak in 200−1200 cm^{-1} indicated the γ phase of Al_2O_3, and the broad peak that is centered at ~1309 cm^{-1} (Figure S3c) can be assigned as the Al−O bending vibrations in the octahedral structure.[32] In the case of the $(60PA\text{-}40CF)_{90}\text{-}Gr_{10}$ sample (Figure 1b), the peaks were observed at 474 cm^{-1} (T_{2g} of CF), 694 cm^{-1} (Al−O bond in tetrahedral AlO_4 in $\gamma\text{-}Al_2O_3$), 1331 cm^{-1} (D band of graphene), and 1578 cm^{-1} (G band of the graphene in-plane vibration mode of sp^2 carbon). The broad peak ranging from ~1000 to 2250 cm^{-1} also indicated the presence of $\gamma\text{-}Al_2O_3$ in the nanocomposite.
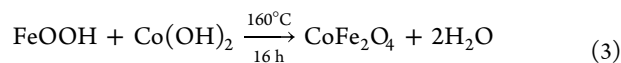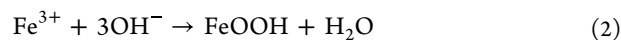
The N_2 adsorption−desorption isotherm of the synthesized materials is shown in Figure 1c, and their specific surface areas and pore diameters are tabulated in Table S1. PA revealed a high specific surface area of ~218 m^2 g^{-1} and an average pore diameter of 4.6 nm. The adsorption−desorption isotherm of PA appeared as a type IV isotherm with a prominent H2 hysteresis loop, indicating its mesoporous nature. In the case of the 60PA-40CF nanocomposite, a type IV isotherm having an H3 hysteresis loop was obtained, which might be due to the blocking of some of the pores of PA as the result of the formation of CF nanoparticles within the pores as well as on the surface of PA. In the case of the $(60PA\text{-}40CF)_{90}\text{-}Gr_{10}$ nanocomposite, where (PA−CF) nanocomposites were immobilized on the surface of nanometer-thin graphene sheets, a type IV isotherm having an H3 hysteresis loop was obtained, and the specific surface area and average pore size were ~199 m^2 g^{-1} and 3.9 nm, respectively.[33]

The microstructures of pure PA, pure CF, graphene, PA−CF, and $(60PA\text{-}40CF)_{90}\text{-}Gr_{10}$ were analyzed using field emission scanning electron microscopy (FESEM) analysis. Figure 2a displays the porous structure of PA with thick walls, indicating the robustness of PA as support. The nanometer-thin sheet structure of pure Gr is shown in Figure S4. The micrograph of pure CF (Figure 2b) showed the loosely agglomerated spherical nanoparticles having an average size of 20−40 nm. In the case of PA−CF, the immobilization of CF nanoparticles within the pores as well as on the surface of PA was observed (Figure 2c). Figure 2d shows the microstructure of $(60PA\text{-}40CF)_{90}\text{-}Gr_{10}$, which illustrates that (60PA-40CF) particles are anchored on the surface of the graphene nanosheets. Figure S5 presents the EDX spectra of (60PA-40CF)$_{90}$-Gr$_{10}$ displaying the characteristic peaks for O, Co, Fe, Al, and C elements, which confirmed their presence in the nanocomposite. Besides, the elemental mapping images of $(60PA\text{-}40CF)_{90}\text{-}Gr_{10}$ (Figure S6) displayed the homogeneous spatial distribution of these elements in the nanocomposite.

The elemental composition and their chemical states in the $(60PA\text{-}40CF)_{90}\text{-}Gr_{10}$ nanocomposite were investigated by X-ray photoelectron spectroscopy (XPS) analysis. The obtained XPS survey spectrum of the $(60PA\text{-}40CF)_{90}\text{-}Gr_{10}$ nanocomposite (Figure S7) showed the distinctive peaks of Al

2p, C 1s, Fe 2p, Co 2p, and O 1s. The deconvoluted Al 2p spectra showed two peaks at 73.7 and 74.7 eV, which were assigned to the typical Al−O bond of $\gamma\text{-}Al_2O_3$ and terminal Al−OH groups, respectively (Figure 3a).[34,35] The spectrum of C 1s showed a peak at 284.8 eV corresponding to sp^2 carbon of graphene (Figure 3b).[36] The curve fitting of the Co 2p peak showed two peaks at 780.9 and 796.6 eV that represents the spin−orbit splitting of Co 2p$_{3/2}$ and Co 2p$_{1/2}$, respectively, and their satellite peaks (sat) were observed at 785.7 and 802.9 eV, respectively (Figure 3c).[31,37] The deconvoluted Fe 2p spectrum is presented in Figure 3d, and the peaks at 710.9 and 724.3 eV were credited to Fe 2p$_{3/2}$ and Fe 2p$_{1/2}$ of Fe^{3+} in the octahedral sites, and two peaks at 712.8 and 726.0 eV were attributed to Fe 2p$_{3/2}$ and Fe 2p$_{1/2}$ of Fe^{3+} in the tetrahedral sites, respectively, whereas the satellite peaks were observed at 718.1 and 733.1 eV.[31,38] As shown in Figure 3e, the O 1s peak curve was deconvoluted to two peaks at 530.0 and 531.5 eV, which arises due to the lattice M−O (M=Co^{2+}, Fe^{3+}, Al^{3+}) bonds and oxygen-containing functional groups, respectively.[31,39]

The aforesaid structural characterizations of the synthesized materials clearly indicated the formation of the desired nanocomposite. In step I, stearic acid (which is a long-chain fatty acid) combined with TEA acts as a pore structure-directing agent. Stearic acid is not very soluble in H_2O, but when combined with TEA, it forms a liquid crystalline phase in an aqueous medium. Simultaneously, TEA forms a coordination complex with Al^{3+} ions and also makes the pH of the reaction medium basic. This causes controlled hydrolysis of the Al−TEA complex, which leads to the precipitation of Al(OH)$_3$ on the liquid crystal template and results in the formation of an organic−inorganic hybrid structure. During the calcination of this hybrid structure, the liquid template decomposes and produces porous $\gamma\text{-}Al_2O_3$. In step II, Co^{2+} and Fe^{3+} ions were adsorbed within the porous structure of $\gamma\text{-}Al_2O_3$. In the presence of NaOH, these ions produce CoFe$_2$O$_4$ nanoparticles (eqs 2 and 3)[40] within the porous structure of $\gamma\text{-}Al_2O_3$, and thus PA−CF nanocomposites are formed. Here, PEG acts as a capping agent and restricts the growth of the size of nanoparticles. In step III, PA−CF particles were anchored on the surface of graphene, which results in the formation of (60PA-40CF)-Gr nanocomposites.

$$Fe^{3+} + 3OH^- \rightarrow FeOOH + H_2O \qquad (2)$$

$$FeOOH + Co(OH)_2 \xrightarrow[16\ h]{160\,°C} CoFe_2O_4 + 2H_2O \qquad (3)$$

3.2. Microwave-Absorption Properties. To determine the microwave-absorption properties of the as-prepared materials, their complex permittivity (ε' and ε'' represent real and imaginary permittivity, respectively) and permeability (real and imaginary permeability are μ' and μ'', respectively) were measured. Generally, the storage capabilities of dielectric and magnetic energy are represented by real parts (ε' and μ') and the dissipation of dielectric and magnetic energy of the samples are expressed by imaginary parts (ε'' and μ'').

Figure S8 displays the change of ε', ε'', μ', and μ'' values of the materials with the change in frequency (in the X-band region, 8.2−12.4 GHz). It was observed that the values of ε' and ε'' of the pure PA, pure CF, and PA−CF composites did not change much with increasing frequency (Figure S8a,b). In PA−CF nanocomposites, with increasing amount of CF, ε' and ε'' values were increased till the CF amount in the
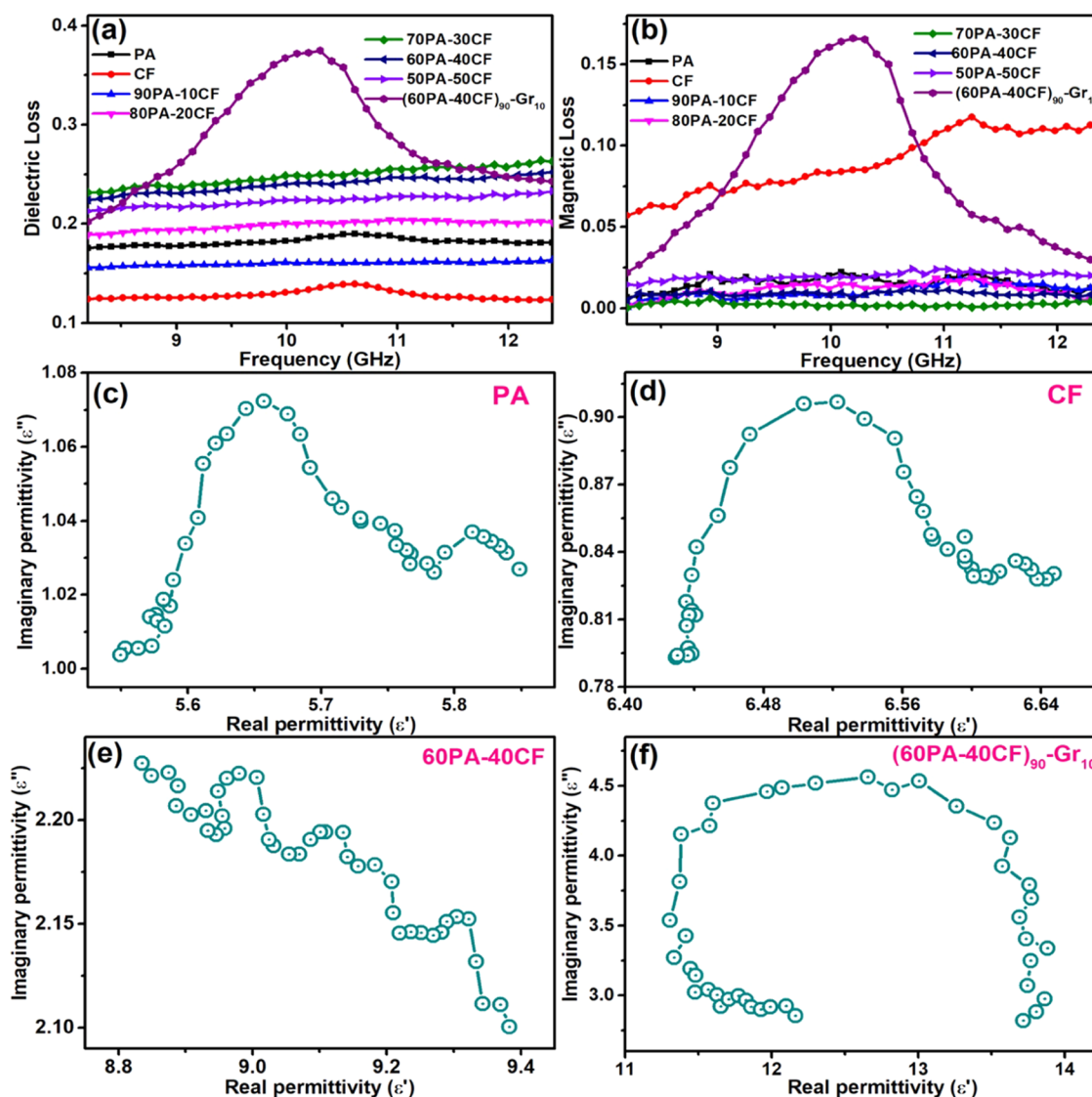
Figure 4. Frequency-dependent (a) dielectric loss and (b) magnetic loss values of the synthesized materials. Typical Cole–Cole semicircles for (c) PA, (d) CF, (e) 60PA-40CF, and (f) (60PA-40CF)$_{90}$-Gr$_{10}$.

nanocomposite reached 40 wt % (60PA-40CF). However, when the composition was 50PA-50CF, any noticeable change in ε' and ε'' was not observed. When Gr was added to the composition of the nanocomposite ((60PA-40CF)$_{90}$-Gr$_{10}$), a significant variation in ε' and ε'' values with increasing frequency was observed. For example, at a frequency of 8.2 GHz, the values of ε' and ε'' of 60PA-40CF were 9.38 and 2.1, respectively, whereas these values were increased to 13.73 and 2.77 for the (60PA-40CF)$_{90}$-Gr$_{10}$ nanocomposite. Moreover, for this Gr-containing nanocomposite, a prominent peak was observed at ~9.97 GHz (Figure S8b). The appearance of this resonance peak can be credited to the displacement current lag generated in the interface between graphene and (60PA-40CF).[41,42] Figure 4a shows the change of the dielectric loss ($\tan \delta_\varepsilon = \varepsilon''/\varepsilon'$) with the variation in frequency. For (60PA-40CF)$_{90}$-Gr$_{10}$, a prominent resonance peak at ~10.1 GHz was observed, which is almost in the same frequency region as it was observed in the ε'' vs frequency plot (Figure S8b). These results suggest that (60PA-40CF)$_{90}$-Gr$_{10}$ possesses better dielectric loss property than those of pure PA, CF, and PA–CF. The conductivity loss and the collective loss of the dipole

polarization and interfacial polarization are the major contributors to the dielectric loss of the graphene-containing nanocomposite. The high conductivity of graphene in (60PA-40CF)$_{90}$-Gr$_{10}$ plays a crucial role in the conductivity loss of (60PA-40CF)$_{90}$-Gr$_{10}$,[9,43–45] and it can be described by the free electron loss theory, which is expressed in eq 4.[9,18,43–46]

$$\varepsilon'' \approx \sigma(T)/2\pi\varepsilon_0 f \tag{4}$$

where $\sigma(T)$ is temperature-dependent electrical conductivity, ε_0 is the dielectric constant in a vacuum, and f is the frequency.[4] The electrical conductivity feature of an MW absorber enhances its ε'' value and thus plays an important role in the dielectric loss property of the absorber. The Debye theory[18] can describe the contribution of the collective loss of the dipole polarization and the interfacial polarization loss in the nanocomposite.[18,46,47] During interaction with an electric field, MW-absorbing materials become polarized. When the electric field is reversed, the polarization is also reversed. The dielectric relaxation loss occurs due to the slower speed of the change in the polarization than the frequency of the rapidly changing electric field. The polarization loss can be categorized

into ionic polarization, electronic polarization, dipole orientation polarization, interfacial polarization (space charge polarization), etc.[48] As ion polarization and electron polarization occur in higher frequency regions (10^3–10^6 GHz), they are not considered in MW absorption. In the high-frequency region, MW absorption mainly occurs through dipole rotation polarization and thermal ion polarization. The presence of defects and residual groups restrict the free movement of dipoles, the bound charges in a dielectric, in the presence of an external electric field. Therefore, a large number of defects and surface functional groups in the materials increase the dipole polarization.[49] In the $(60PA\text{-}40CF)_{90}\text{-}Gr_{10}$ nanocomposite, the porous structure of PA provides a significant number of defects as well as air–material interfaces due to which many dipole pairs generate under an applied electromagnetic field and thus enhance the internal polarization loss. Due to the immobilization of PA–CF on the surface of graphene, a large number of defects are created. Moreover, the interfacial polarization emanates from the interface between (60PA-40CF) and graphene. In this heterogeneous structure, interfacial polarization and related relaxation processes also play important roles. In the interfaces, the generation of macro dipole moments due to the accumulation and uneven distribution of space charge causes effective absorption of incident EM energy.[46,47,50] Debye dipolar relaxation significantly impacts the permittivity behaviors of microwave absorbers.

According to Debye dipolar relaxation, the relative complex permittivity ε_r is expressed as eq 5 [18,46,50−52]

$$\varepsilon_r = \varepsilon' + i\varepsilon'' = \varepsilon_\infty + \frac{\varepsilon_s - \varepsilon_\infty}{1 + i2\pi f\tau_0} \tag{5}$$

where ε_∞ represents the stationary permittivity and optical dielectric constant at a high-frequency limit, τ_0 is polarization relaxation time, and f is the frequency. Equations 6 and 7 can be derived from eq 5.

$$\varepsilon' = \varepsilon_\infty + \frac{\varepsilon_s - \varepsilon_\infty}{1 + (i2\pi f\tau_0)^2} \tag{6}$$

$$\varepsilon'' = \frac{2\pi f\tau_0(\varepsilon_s - \varepsilon_\infty)}{1 + (2\pi f\tau_0)^2} + \frac{\sigma(T)}{2\pi f\varepsilon_0} \tag{7}$$

From eqs 6 and 7, the correlation of ε' and ε'' can be expressed as eq 8.

$$\left(\varepsilon' - \frac{\varepsilon_s + \varepsilon_\infty}{2}\right)^2 + (\varepsilon'')^2 = \left(\frac{\varepsilon_s - \varepsilon_\infty}{2}\right)^2 \tag{8}$$

The ε'' vs ε' curve, which is known as the Cole–Cole plot, provides information to assess the Debye dipolar relaxation process of microwave absorbers and can be derived based on the Debye dipole relaxation theory (eq 8). Each Cole–Cole semicircle signifies one Debye relaxation process caused by heterogeneous interface polarization, and the presence of more semicircles indicates multiple Debye dipolar relaxation processes.[48] Cole–Cole plots of the synthesized materials are shown in Figures 4c–f and S9, and the number of semicircles in the Cole–Cole plot was found to be increased in the order of CF ≈ PA < 60PA-40CF < $(60PA\text{-}40CF)_{90}\text{-}Gr_{10}$. This observation indicates that multiple Debye dipolar relaxation processes generate when the $(60PA\text{-}40CF)_{90}\text{-}Gr_{10}$ nanocomposite interacts with MW radiation. In $(60PA\text{-}40CF)_{90}\text{-}Gr_{10}$, the interfaces exist between PA–CF, PA–Gr, CF–Gr, and (PA–CF)–Gr. Under alternating electromagnetic radia-

tion, these interfaces cause a delay in induced charges, which interact with the externally applied field and result in relaxation and transformation of the electromagnetic energy to thermal energy. Moreover, the defects present in PA–CF and $(60PA\text{-}40CF)_{90}\text{-}Gr_{10}$ lead to self-doping.[18,53] This factor provides supplementary carriers between the interfaces and benefits the Debye relaxation. In addition to this Debye relaxation effect, the aggregation of bound charges at the heterogeneous interface also originates the Maxwell–Wagner relaxation, which may increase the EM absorption of the $(60PA\text{-}40CF)_{90}\text{-}Gr_{10}$ nanocomposite.[18,46,50]

Magnetic loss is another significant parameter that enhances the EM wave absorption in the materials. Figure S8c,d show the variation of μ' and μ'' with varying frequency for all of the samples. Due to its magnetic character, pure CF showed much higher values than those of the other synthesized materials. With the increase in wt % of CF in the PA–CF nanocomposites, the values of μ' and μ'' were increased and the highest value was observed for the 60PA-40CF nanocomposite. For each of the PA–CF nanocomposites, the change of μ' and μ'' with increasing frequency was not significant. In the case of the $(60PA\text{-}40CF)_{90}\text{-}Gr_{10}$ nanocomposite, the values of μ' and μ'' were observed to be higher than those of PA–CF composites.

Figure S8d depicts the presence of a broad peak centered at 10.29 GHz in μ'' vs frequency plot of $(60PA\text{-}40CF)_{90}\text{-}Gr_{10}$. Figure 4b displays the variation of the magnetic tangent loss ($\tan \delta_\mu = \mu''/\mu'$) with varying frequencies of the synthesized materials. Generally, the magnetic loss occurs due to exchange resonances, natural resonances, and eddy current loss in the microwave band. Tan δ_μ is related to the hysteresis loss, which signifies the energy dissipation of a static hysteresis loop, eddy current loss due to the electrical resistivity, and a residual loss, which is associated with the magnetic domain wall, spin rotational resonances, and natural loss.[18,54] However, generally, hysteresis loss is negligible in a weak field.[18] The domain wall effect usually becomes appreciable in the megahertz frequency range.[55] The eddy current loss, natural resonance, and exchange resonance can be considered the more effective element.[56] The eddy current loss is determined using eqs 9 and 10 [12,18,46,52,53]

$$\mu'' \approx 2\pi\mu_0(\mu')^2\sigma d^2f/3 \tag{9}$$

$$C_0 = \mu''(\mu')^{-2}f^{-1} = 2\pi\mu_0 d^2\sigma \tag{10}$$

where μ_0 is permeability in a vacuum, σ is the electrical conductivity of the composite, d is the thickness of the absorber, and C_0 is the eddy current coefficient. When there is no alteration in the value of $\mu''(\mu')^{-2}f^{-1}$ with varying frequencies, then it can be expected that the eddy current loss is contributing toward magnetic loss. Another vital factor that contributes to magnetic loss is the natural resonance, which generally occurs at lower frequencies and can be expressed as eqs 11–13 [12,18,46,57]

$$2\pi f_r = \gamma H_a \tag{11}$$

$$H_a = 4|K_1|/3\mu_0 M_s \tag{12}$$

$$K_1 = \mu_0 M_s H_c/2 \tag{13}$$

where f_r represents the resonance frequency, H_a is anisotropy energy, γ is the gyromagnetic ratio, $|K_1|$ is anisotropy coefficient, M_s is saturation magnetization, μ_0 stands for
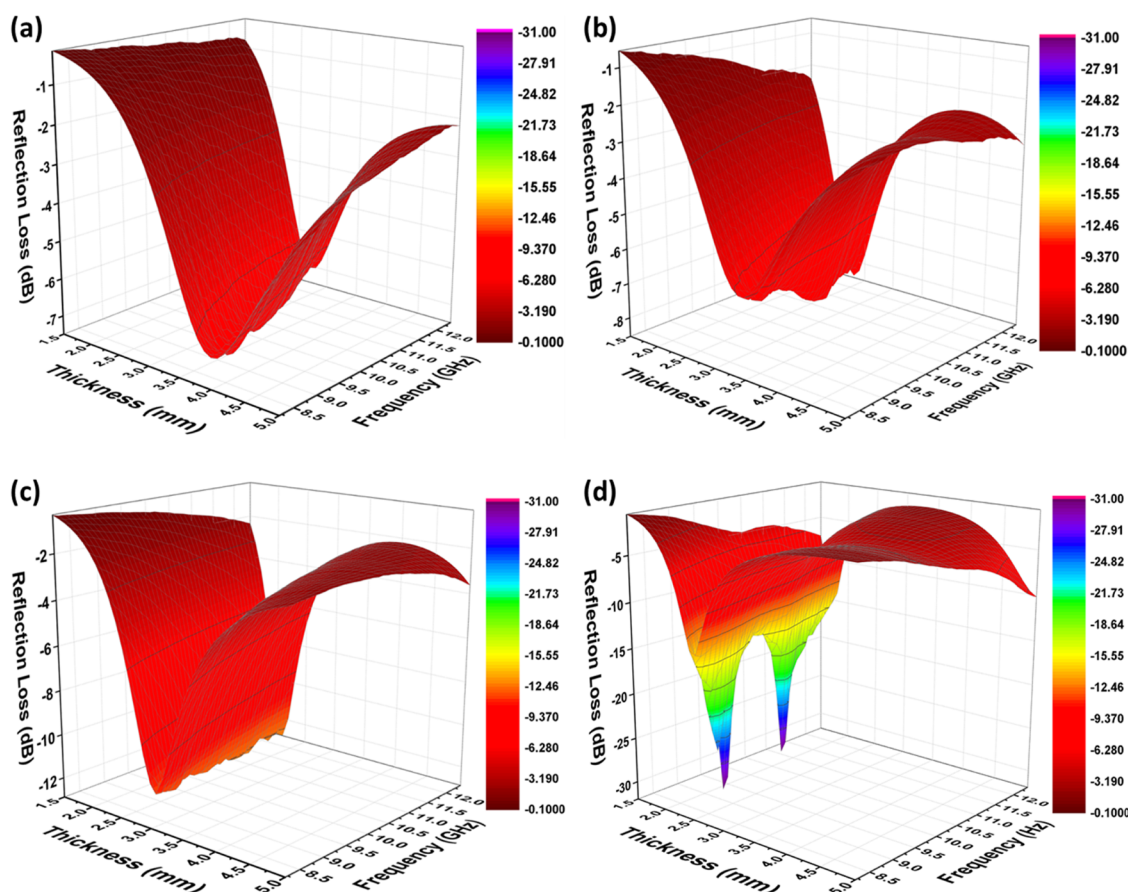
Figure 5. 3D thickness-dependent RL plots of (a) PA, (b) CF, (c) 60PA-40CF, and (d) $(60PA-40CF)_{90}$-Gr_{10}.

permeability in free space $(4\pi \times 10^{-7}$ H m$^{-1})$, and H_C is coercivity.

Figure 4b shows that the magnetic loss of pure CF was much greater than that of PA−CF composites. This could be due to the presence of nonmagnetic PA, which reduces the magnetic character of the PA−CF composite as compared to the pure CF. In the case of the $(60PA-40CF)_{90}$-Gr_{10} sample, a broad peak centered at ∼10.2 GHz was observed, which is an indication of the involvement of exchange resonance loss phenomena in the magnetic loss of the nanocomposite. Figure S10 displays the change of the eddy current coefficient (C_0) with the variation in frequency. Here, for pure CF and PA−CF composites, as no noticeable change in the C_0 with increasing frequency was observed, it was considered that eddy current loss plays a crucial role in the MW absorption for these samples.[4] In the case of $(60PA-40CF)_{90}$-Gr_{10}, the value of C_0 changes with the variation of frequency, and a broad peak centered at ∼10 GHz was observed (Figure S10). Hence, in this case, eddy current loss may not play a crucial role and the exchange resonance phenomenon commits significantly to the magnetic loss of this nanocomposite.

The values of reflection loss (RL) with changing frequency can be calculated from the complex permittivity $(\varepsilon_r = \varepsilon' - j\varepsilon'')$ and complex permeability $(\mu_r = \mu' - j\mu'')$ using the single-layered plane wave-absorber model proposed by Naito and Suetake (eqs 14 and 15)[58,59]

$$Z_{in} = Z_0(\mu_r/\varepsilon_r)^{1/2}\tan h\left[j\left(\frac{2\pi fd}{c}\right)(\mu_r \cdot \varepsilon_r)^{1/2}\right] \quad (14)$$

$$RL = 20\log\left|\frac{Z_{in} - Z_0}{Z_{in} - Z_0}\right| \quad (15)$$

In eqs 14 and 15, Z_{in} is the input impedance of the absorber, Z_0 is the impedance of free space, f is the microwave frequency, d is the absorber thickness, j is the imaginary unit, and c is the velocity of magnetic waves in free space.

Figure 5 displays the three-dimensional plots for pure PA, pure CF, 60PA-40CF, and $(60PA-40CF)_{90}$-Gr_{10} nanocomposites showing the frequency-dependent RL values with the variation in absorber thickness. Three-dimensional plots of 90PA-10CF, 80PA-20CF, 70PA-30CF, and 50PA-50CF are presented in Figure S11, and two-dimensional plots of all of the as-prepared materials are presented in Figures S12−S16. From these plots, the following key points were noted: (i) pure CF manifested a minimum RL of ∼−8.5 dB (∼86%) at 11.23 GHz when the thickness was 2.5 mm. (ii) Pure PA shows the lowest RL of ∼−7.44 dB (∼82%) at 10.37 GHz and thickness was 3.2 mm. (iii) In the PA−CF nanocomposites, the incorporation of CF nanoparticles within the porous Al_2O_3 matrix enhances the minimum RL value, and with the increase in the CF content in PA−CF, the minimum RL value increases till 60 wt % of CF (60PA-40CF). Beyond the incorporation of 40 wt % CF, minimum RL decreases (Table S2). The highest minimum RL value of −12.73 dB (∼-94.5%) was exhibited by the 60PA-40CF nanocomposite at 11.21 GHz when the absorber thickness was 2.3 mm. The effective bandwidth (RL < −10 dB) was found to be in the frequency range from 8.2 to 12.4 GHz for this sample. (iv) As among the PA−CF nanocomposites, 60PA-40CF displayed the best microwave-

absorption properties, we have synthesized nanocomposites having various amounts of 60PA-40CF and graphene, where graphene amounts varied from 10 to 90 wt %. Among these graphene-containing nanocomposites, when microwave-absorption measurement experiments were performed, we obtained reasonable data only for $(60PA-40CF)_{90}$-Gr_{10}. When in the composite the graphene content was more than 10 wt %, due to the high conductivity of graphene generation, an excessive amount of eddy current loss occurs, which causes high reflection of incident MW and results in poor impedance matching and consequently weakening the MW-absorption property of the composites.[60] Therefore, any meaningful result was not obtained for the graphene-rich composites (Figure S15b). $(60PA-40CF)_{90}$-Gr_{10} exhibited the maximum RL value of ∼−30.68 dB (∼99.9% absorption) at 10.71 GHz as well as at 9.04 GHz with matching thicknesses of 2.0 and 2.3 mm, respectively. Moreover, it also showed an effective bandwidth range from 8.2 to 12.4 GHz.

The attenuation constant (α) is also an important parameter that indicates the performance of a microwave absorber and can be calculated using eq 16. High dielectric loss and magnetic loss provide a high value of α and signify the capability of the absorber to dissipate microwave.[61−64]

$$\alpha = \frac{\sqrt{2}\,\pi f}{c}$$
$$\times \sqrt{(\mu''\varepsilon'' - \mu'\varepsilon') + \sqrt{(\mu''\varepsilon'' - \mu'\varepsilon')^2 + (\mu'\varepsilon'' + \mu''\varepsilon')^2}} \tag{16}$$

Figure S17 displays the attenuation constant curve for PA, CF, 60PA-40CF, and $(60PA-40CF)_{90}$-Gr_{10}. The higher values of α for the $(60PA-40CF)_{90}$-Gr_{10} nanocomposite than the PA, CF, and 60PA-40CF reveal that this nanocomposite possesses stronger capability. Significantly high values of RL and α manifest the competence of the $(60PA-40CF)_{90}$-Gr_{10} nanocomposite as a strong MW absorber in the X-band region. Some of the factors that play critical roles in the enhanced microwave-absorption properties of the $(60PA-40CF)_{90}$-Gr_{10} nanocomposite are: (i) The presence of interfaces between PA−air, PA−CF, PA−Gr, CF−Gr, (PA−CF)−Gr generates interfacial polarization and hence induces Debye relaxation, (ii) the porous structure of PA helps MW absorption via multiple scattering within the pores, (iii) the high surface area of graphene and PA enhances MW absorption, (iv) the high conductivity of graphene produces conductivity loss, and (v) due to the magnetic nature of CF nanoparticles, their presence in the composite results in a magnetic loss. Scheme 2 illustrates the MW-absorption mechanism of the $(60PA-40CF)_{90}$-Gr_{10} nanocomposite.

4. CONCLUSIONS

In summary, a nanocomposite composed of CF, PA, and Gr was successfully developed and tested as an efficient microwave-absorbing material. It was observed that the growth of CF nanoparticles within the porous structure of PA in (PA−CF) nanocomposites caused a significant improvement in microwave-absorption properties compared to pure PA and pure CF. Further enhancement of microwave-absorption property was observed when the PA−CF nanocomposite was immobilized on the surface of graphene. The synergistic effect originated from the presence of PA with high dielectric property, magnetic nature of CF, and high electric conductance, as well as high surface area of Gr in the (60PA-

Scheme 2. MW-Absorption Mechanism of the $(60PA-40CF)_{90}$-Gr_{10} Nanocomposite
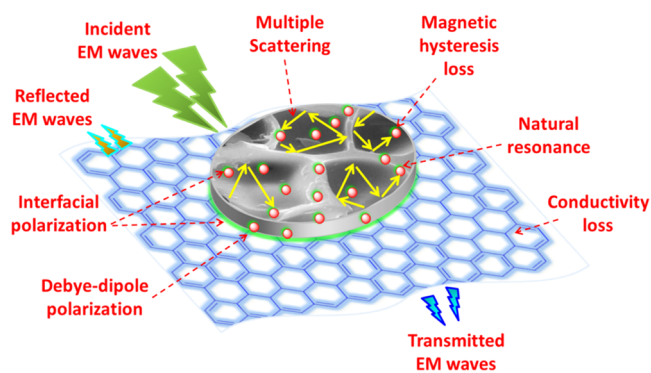
$40CF)_{90}$-Gr_{10} nanocomposite resulted in the excellent microwave-absorption properties of this nanocomposite in the X-band region. The $(60PA-40CF)_{90}$-Gr_{10} nanocomposite possessed a broad effective bandwidth range from 8.2 to 12.4 GHz and exhibited a reflection loss (RL) value of ∼−30.68 dB (∼99.9% absorption) at 10.71 and 9.04 GHz with matching thicknesses of 2.0 and 2.3 mm, respectively. The work depicted here successfully presents the design and synthesis of a microwave absorber $(60PA-40CF)_{90}$-Gr_{10}, which exhibits microwave-absorption properties that are superior to many microwave-absorbing materials (Table S3). This fact clearly illustrates the potentiality of $(60PA-40CF)_{90}$-Gr_{10} as a lightweight, high-performance microwave absorber in the X-band region, which makes it an attractive material in the field of stealth technologies.

■ ASSOCIATED CONTENT

ⓈI Supporting Information

The Supporting Information is available free of charge at https://pubs.acs.org/doi/10.1021/acsomega.2c03648.

Materials and methods; characterization details and instruments used; XRD patterns of (a) PA, (b) CF, (c) 60PA-40CF, (d) Gr, $(60PA-40CF)_{10}$-Gr_{90}, $(60PA-40CF)_{25}$-Gr_{75}, $(60PA-40CF)_{50}$-Gr_{50}, and $(60PA-40CF)_{75}$-Gr_{25}; Raman spectra of (a) Gr, (b) CF, and (c) PA; BET surface area data (Table S1); FESEM micrograph of Gr; EDS spectra and elemental mapping images of $(60PA-40CF)_{90}$-Gr_{10}; XPS survey spectrum of $(60PA-40CF)_{90}$-Gr_{10}; frequency dependence: (a) real part and (b) imaginary part of relative complex permittivity, (c) real part, and (d) imaginary part of relative complex permeability values of the synthesized materials; Cole−Cole semicircles for (a) 90PA-10CF, (b) 80PA-20CF, (c) 70PA-30CF, and (d) 50PA-50CF; plots of $\mu''(\mu')^{-2}f^{-1}$ vs frequency for the synthesized materials; 3D thickness-dependent RL plots of (a) 90PA-10CF, (b) 80PA-20CF, (c) 70PA-30CF, and (d) 50PA-50CF; minimum reflection loss values of (a) PA, (b) CF, (c) 90PA-10CF, (d) 80PA-20CF, (e) 70PA-30CF, (f) 60PA-40CF, (g) 50PA-50CF, (h) $(60PA-40CF)_{75}$-Gr_{25}, and (i) $(60PA-40CF)_{90}$-Gr_{10}; attenuation constant (α) vs frequency curves of the materials; microwave-absorption data (Table S2); and comparison table (Table S3) (PDF)

■ AUTHOR INFORMATION

Corresponding Author

Narendra Nath Ghosh − *Nano-Materials Lab, Department of Chemistry, Birla Institute of Technology and Science, Sancoale, Goa 403726, India;* ◉ orcid.org/0000-0002-8338-7292; Phone: +91 832 2580318/25570339; Email: naren70@yahoo.com

Authors

Debika Gogoi − *Nano-Materials Lab, Department of Chemistry, Birla Institute of Technology and Science, Sancoale, Goa 403726, India*

Raghavendra Korde − *Nano-Materials Lab, Department of Chemistry, Birla Institute of Technology and Science, Sancoale, Goa 403726, India*

Virendra Singh Chauhan − *Defence Lab, Defence Research and Development Organisation, Jodhpur 342011, India*

Manoj Kumar Patra − *Defence Lab, Defence Research and Development Organisation, Jodhpur 342011, India*

Debmalya Roy − *Defence Materials and Stores Research & Development Establishment (DMSRDE) DRDO, Ministry of Defence, Government of India, PO DMSRDE, Kanpur 208013, India;* ◉ orcid.org/0000-0003-3629-5309

Manash R. Das − *Advanced Materials Group, Materials Sciences and Technology Division, CSIR-North East Institute of Science and Technology, Jorhat 785006 Assam, India; Academy of Scientific and Innovative Research (AcSIR), Ghaziabad 201002, India;* ◉ orcid.org/0000-0002-6317-7933

Complete contact information is available at:
https://pubs.acs.org/10.1021/acsomega.2c03648

Notes

The authors declare no competing financial interest.

■ REFERENCES

(1) Kim, H.; Park, S.; Kim, S.; Seo, Y. Microwave absorption and shielding property of Fe-Si-Al alloy/MWCNT/polymer nanocomposites. *Langmuir* **2019**, *35*, 6950−6955.

(2) Liu, Q.; Cao, Q.; Zhao, X.; Bi, H.; Wang, C.; Wu, D. S.; Che, R. Insights into size-dominant magnetic microwave absorption properties of CoNi microflowers via off-axis electron holography. *ACS Appl. Mater. Interfaces* **2015**, *7*, 4233−4240.

(3) Cao, M.-S.; Cai, Y.-Z.; He, P.; Shu, J.-C.; Cao, W.-Q.; Yuan, J. 2D MXenes: electromagnetic property for microwave absorption and electromagnetic interference shielding. *Chem. Eng. J.* **2019**, *359*, 1265−1302.

(4) Moitra, D.; Dhole, S.; Ghosh, B. K.; Chandel, M.; Jani, R. K.; Patra, M. K.; Vadera, S. R.; Ghosh, N. N. Synthesis and Microwave Absorption Properties of BiFeO₃ Nanowire-RGO Nanocomposite and First-Principles Calculations for Insight of Electromagnetic Properties and Electronic Structures. *J. Phys. Chem. C* **2017**, *121*, 21290−21304.

(5) Huang, Y.; Wang, Y.; Li, Z.; Yang, Z.; Shen, C.; He, C. Effect of pore morphology on the dielectric properties of porous carbons for microwave absorption applications. *J. Phys. Chem. C* **2014**, *118*, 26027−26032.

(6) Wang, S.; Li, D.; Zhou, Y.; Jiang, L. Hierarchical Ti₃C₂Tₓ MXene/Ni Chain/ZnO Array Hybrid Nanostructures on Cotton Fabric for Durable Self-Cleaning and Enhanced Microwave Absorption. *ACS Nano* **2020**, *14*, 8634−8645.

(7) Zhan, R.; Zhang, J.; Gao, Q.; Jia, Q.; Zhang, Z.; Zhang, G.; Gu, W. Microwave Absorption Performance of Single-Layer and Multi-Layer Structures Prepared by CNTs/Fe₃O₄ Nonwoven Materials. *Crystals* **2021**, *11*, No. 1000.

(8) Jia, Z.; Lan, D.; Lin, K.; Qin, M.; Kou, K.; Wu, G.; Wu, H. Progress in low-frequency microwave absorbing materials. *J. Mater. Sci. Mater. Electron.* **2018**, *29*, 17122−17136.

(9) Yang, H.-J.; Cao, W.-Q.; Zhang, D.-Q.; Su, T.-J.; Shi, H.-L.; Wang, W.-Z.; Yuan, J.; Cao, M.-S. NiO hierarchical nanorings on SiC: enhancing relaxation to tune microwave absorption at elevated temperature. *ACS Appl. Mater. Interfaces* **2015**, *7*, 7073−7077.

(10) Zhou, J.; Tao, J.; Yao, Z.; Xu, L.; Li, Z.; Chen, P. Ag Nanoparticles Embedded in Multishell Carbon Nanoparticles for Microwave Absorption. *ACS Appl. Nano Mater.* **2021**, *4*, 5425−5436.

(11) Liu, J.; Cao, M.-S.; Luo, Q.; Shi, H.-L.; Wang, W.-Z.; Yuan, J. Electromagnetic property and tunable microwave absorption of 3D nets from nickel chains at elevated temperature. *ACS Appl. Mater. Interfaces* **2016**, *8*, 22615−22622.

(12) Zhang, X.-J.; Wang, G.-S.; Cao, W.-Q.; Wei, Y.-Z.; Liang, J.-F.; Guo, L.; Cao, M.-S. Enhanced microwave absorption property of reduced graphene oxide (RGO)-MnFe₂O₄ nanocomposites and polyvinylidene fluoride. *ACS Appl. Mater. Interfaces* **2014**, *6*, 7471−7478.

(13) Yuan, X.; Cheng, L.; Zhang, L. Influence of temperature on dielectric properties and microwave absorbing performances of TiC nanowires/SiO₂ composites. *Ceram. Int.* **2014**, *40*, 15391−15397.

(14) Green, M.; Chen, X. Recent progress of nanomaterials for microwave absorption. *J. Materiomics* **2019**, *5*, 503−541.

(15) Gao, L.; Zhou, W.; Luo, F.; Zhu, D.; Wang, J. Dielectric and microwave absorption properties of KNN/Al₂O₃ composite ceramics. *Ceram. Int.* **2017**, *43*, 12731−12735.

(16) Liu, X.; Lu, X.; Song, Y.; Xia, S.; Ren, R.; Wang, Y.; Zhao, D.; Wang, M. Plasma-sprayed graphene nanosheets/ZnO/Al₂O₃ coatings with highly efficient microwave absorption properties. *J. Therm. Spray Technol.* **2021**, *30*, 1524−1534.

(17) Kumar, H.; Srivastava, R.; Negi, P.; Agrawal, H.; Asokan, K. Dielectric behaviour of cobalt ferrite nanoparticles. *Int. J. Electr. Electron. Eng.* **2013**, *2*, 59−66.

(18) Liu, P.; Yao, Z.; Zhou, J.; Yang, Z.; Kong, L. B. Small magnetic Co-doped NiZn ferrite/graphene nanocomposites and their dual-region microwave absorption performance. *J. Mater. Chem. C* **2016**, *4*, 9738−9749.

(19) Wang, L.; Huang, Y.; Sun, X.; Huang, H.; Liu, P.; Zong, M.; Wang, Y. Synthesis and microwave absorption enhancement of graphene@Fe₃O₄@SiO₂@NiO nanosheet hierarchical structures. *Nanoscale* **2014**, *6*, 3157−3164.

(20) Wang, M.; Zhang, Y.; Dong, C.; Chen, G.; Guan, H. Preparation and electromagnetic shielding effectiveness of cobalt ferrite nanoparticles/carbon nanotubes composites. *Nanomater. Nanotechnol.* **2019**, *9*, No. 1847980419837821.

(21) Ma, T.; Cui, Y.; Liu, L.; Luan, H.; Ge, J.; Ju, P.; Meng, F.; Wang, F. Tailored design of p-phenylenediamine functionalized graphene decorated with cobalt ferrite for microwave absorption. *RSC Adv.* **2020**, *10*, 31848−31855.

(22) Song, W.-L.; Guan, X.-T.; Fan, L.-Z.; Zhao, Y.-B.; Cao, W.-Q.; Wang, C.-Y.; Cao, M.-S. Strong and thermostable polymeric graphene/silica textile for lightweight practical microwave absorption composites. *Carbon* **2016**, *100*, 109−117.

(23) Sultanov, F.; Daulbayev, C.; Bakbolat, B.; Daulbayev, O. Advances of 3D graphene and its composites in the field of microwave absorption. *Adv. Colloid Interface Sci.* **2020**, *285*, No. 102281.

(24) Naik, B.; Prasad, V.; Ghosh, N. Development of a simple aqueous solution based chemical method for synthesis of mesoporous

γ-alumina powders with disordered pore structure. *J. Porous Mater.* **2010**, *17*, 115−121.

(25) Gogoi, D.; Makkar, P.; Ghosh, N. N. Solar Light-Irradiated Photocatalytic Degradation of Model Dyes and Industrial Dyes by a Magnetic $CoFe_2O_4$-gC_3N_4 S-Scheme Heterojunction Photocatalyst. *ACS Omega* **2021**, *6*, 4831−4841.

(26) Naik, B.; Prasad, V. S.; Ghosh, N. N. Preparation of Ag nanoparticle loaded mesoporous γ-alumina catalyst and its catalytic activity for reduction of 4-nitrophenol. *Powder Technol.* **2012**, *232*, 1−6.

(27) Gogoi, D.; Das, M. R.; Ghosh, N. N. $CoFe_2O_4$ Hollow Spheres-Decorated Three-Dimensional rGO Sponge for Highly Efficient Electrochemical Charge Storage Devices. *ACS Omega* **2022**, *7*, 11305−11319.

(28) Rao, C. N. R.; Biswas, K.; Subrahmanyam, K.; Govindaraj, A. Graphene, the new nanocarbon. *J. Mater. Chem.* **2009**, *19*, 2457−2469.

(29) Wang, H.; Wang, Y.; Cao, X.; Feng, M.; Lan, G. Vibrational properties of graphene and graphene layers. *J. Raman Spectrosc.* **2009**, *40*, 1791−1796.

(30) Supriya, S.; Kumar, S.; Kar, M. Structural and Electrical Properties of CFO Nanoparticle-Filled PVA. *J. Electron. Mater.* **2019**, *48*, 3612−3623.

(31) Gogoi, D.; Makkar, P.; Das, M. R.; Ghosh, N. N. $CoFe_2O_4$ Nanoparticle Decorated Hierarchical Biomass Derived Porous Carbon Based Nanocomposites for High-Performance All-Solid-State Flexible Asymmetric Supercapacitor Devices. *ACS Appl. Electron. Mater.* **2022**, *4*, 795−806.

(32) Baronskiy, M.; Rastorguev, A.; Zhuzhgov, A.; Kostyukov, A.; Krivoruchko, O.; Snytnikov, V. Photoluminescence and Raman spectroscopy studies of low-temperature γ-Al_2O_3 phases synthesized from different precursors. *Opt. Mater.* **2016**, *53*, 87−93.

(33) Thommes, M.; Kaneko, K.; Neimark, A. V.; Olivier, J. P.; Rodriguez-Reinoso, F.; Rouquerol, J.; Sing, K. S. Physisorption of gases, with special reference to the evaluation of surface area and pore size distribution (IUPAC Technical Report). *Pure Appl. Chem.* **2015**, *87*, 1051−1069.

(34) Kim, H. J.; Kearney, K. L.; Le, L. H.; Pekarek, R. T.; Rose, M. J. Platinum-enhanced electron transfer and surface passivation through ultrathin film aluminum oxide (Al_2O_3) on Si (111)-CH_3 photo-electrodes. *ACS Appl. Mater. Interfaces* **2015**, *7*, 8572−8584.

(35) Bing, J.; Hu, C.; Nie, Y.; Yang, M.; Qu, J. Mechanism of catalytic ozonation in Fe_2O_3/Al_2O_3@SBA-15 aqueous suspension for destruction of ibuprofen. *Environ. Sci. Technol.* **2015**, *49*, 1690−1697.

(36) Reddy, A. L. M.; Srivastava, A.; Gowda, S. R.; Gullapalli, H.; Dubey, M.; Ajayan, P. M. Synthesis of nitrogen-doped graphene films for lithium battery application. *ACS Nano* **2010**, *4*, 6337−6342.

(37) Nappini, S.; Magnano, E.; Bondino, F.; Pis, I.; Barla, A.; Fantechi, E.; Pineider, F.; Sangregorio, C.; Vaccari, L.; Venturelli, L.; Baglioni, P. Surface charge and coating of $CoFe_2O_4$ nanoparticles: evidence of preserved magnetic and electronic properties. *J. Phys. Chem. C* **2015**, *119*, 25529−25541.

(38) Gogoi, D.; Karmur, R. S.; Das, M. R.; Ghosh, N. N. Cu and $CoFe_2O_4$ nanoparticles decorated hierarchical porous carbon: An excellent catalyst for reduction of nitroaromatics and microwave-assisted antibiotic degradation. *Appl. Catal., B* **2022**, *312*, No. 121407.

(39) Gogoi, D.; Karmur, R. S.; Das, M. R.; Ghosh, N. N. A high-performance flexible energy storage device from biomass-derived porous carbon supported $MnCo_2O_4$ nanorods and MnO_2 nanoscales. *Sustainable Energy Fuels* **2022**, *6*, No. 3599.

(40) Moitra, D.; Chandel, M.; Ghosh, B. K.; Jani, R. K.; Patra, M. K.; Vadera, S. R.; Ghosh, N. N. A simple 'in situ' co-precipitation method for the preparation of multifunctional $CoFe_2O_4$-reduced graphene oxide nanocomposites: excellent microwave absorber and highly efficient magnetically separable recyclable photocatalyst for dye degradation. *RSC Adv.* **2016**, *6*, 76759−76772.

(41) Zhang, X. F.; Dong, X.; Huang, H.; Lv, B.; Lei, J.; Choi, C. Microstructure and microwave absorption properties of carbon-coated iron nanocapsules. *J. Phys. D: Appl. Phys.* **2007**, *40*, No. 5383.

(42) Watts, P.; Ponnampalam, D.; Hsu, W.; Barnes, A.; Chambers, B. The complex permittivity of multi-walled carbon nanotube−polystyrene composite films in X-band. *Chem. Phys. Lett.* **2003**, *378*, 609−614.

(43) Cao, M.-S.; Song, W.-L.; Hou, Z.-L.; Wen, B.; Yuan, J. The effects of temperature and frequency on the dielectric properties, electromagnetic interference shielding and microwave-absorption of short carbon fiber/silica composites. *Carbon* **2010**, *48*, 788−796.

(44) Chen, Y.-J.; Xiao, G.; Wang, T.-S.; Ouyang, Q.-Y.; Qi, L.-H.; Ma, Y.; Gao, P.; Zhu, C.-L.; Cao, M.-S.; Jin, H.-B. Porous Fe_3O_4/carbon core/shell nanorods: synthesis and electromagnetic properties. *J. Phys. Chem. C* **2011**, *115*, 13603−13608.

(45) Ramo, S.; Whinnery, J. R.; Van Duzer, T. *Fields and Waves in Communication Electronics*; John Wiley & Sons, 1994.

(46) Jian, X.; Wu, B.; Wei, Y.; Dou, S. X.; Wang, X.; He, W.; Mahmood, N. Facile synthesis of Fe_3O_4/GCs composites and their enhanced microwave absorption properties. *ACS Appl. Mater. Interfaces* **2016**, *8*, 6101−6109.

(47) Cao, J.; Fu, W.; Yang, H.; Yu, Q.; Zhang, Y.; Liu, S.; Sun, P.; Zhou, X.; Leng, Y.; Wang, S.; et al. Large-scale synthesis and microwave absorption enhancement of actinomorphic tubular ZnO/$CoFe_2O_4$ nanocomposites. *J. Phys. Chem. B* **2009**, *113*, 4642−4647.

(48) Zeng, X.; Cheng, X.; Yu, R.; Stucky, G. D. Electromagnetic microwave absorption theory and recent achievements in microwave absorbers. *Carbon* **2020**, *168*, 606−623.

(49) Quan, B.; Liang, X.; Ji, G.; Cheng, Y.; Liu, W.; Ma, J.; Zhang, Y.; Li, D.; Xu, G. Dielectric polarization in electromagnetic wave absorption: review and perspective. *J. Alloys Compd.* **2017**, *728*, 1065−1075.

(50) Chen, D.; Wang, G.-S.; He, S.; Liu, J.; Guo, L.; Cao, M.-S. Controllable fabrication of mono-dispersed RGO-hematite nano-composites and their enhanced wave absorption properties. *J. Mater. Chem. A* **2013**, *1*, 5996−6003.

(51) Chen, Y.-H.; Huang, Z.-H.; Lu, M.-M.; Cao, W.-Q.; Yuan, J.; Zhang, D.-Q.; Cao, M.-S. 3D Fe_3O_4 nanocrystals decorating carbon nanotubes to tune electromagnetic properties and enhance microwave absorption capacity. *J. Mater. Chem. A* **2015**, *3*, 12621−12625.

(52) Li, N.; Huang, G.-W.; Li, Y.-Q.; Xiao, H.-M.; Feng, Q.-P.; Hu, N.; Fu, S.-Y. Enhanced microwave absorption performance of coated carbon nanotubes by optimizing the Fe_3O_4 nanocoating structure. *ACS Appl. Mater. Interfaces* **2017**, *9*, 2973−2983.

(53) He, J.-Z.; Wang, X.-X.; Zhang, Y.-L.; Cao, M.-S. Small magnetic nanoparticles decorating reduced graphene oxides to tune the electromagnetic attenuation capacity. *J. Mater. Chem. C* **2016**, *4*, 7130−7140.

(54) Lu, B.; Dong, X.; Huang, H.; Zhang, X.; Zhu, X.; Lei, J.; Sun, J. Microwave absorption properties of the core/shell-type iron and nickel nanoparticles. *J. Magn. Magn. Mater.* **2008**, *320*, 1106−1111.

(55) Lv, H.; Zhang, H.; Ji, G.; Xu, Z. J. Interface strategy to achieve tunable high frequency attenuation. *ACS Appl. Mater. Interfaces* **2016**, *8*, 6529−6538.

(56) Wang, G.; Gao, Z.; Wan, G.; Lin, S.; Yang, P.; Qin, Y. High densities of magnetic nanoparticles supported on graphene fabricated by atomic layer deposition and their use as efficient synergistic microwave absorbers. *Nano Res.* **2014**, *7*, 704−716.

(57) Zong, M.; Huang, Y.; Zhao, Y.; Sun, X.; Qu, C.; Luo, D.; Zheng, J. Facile preparation, high microwave absorption and microwave absorbing mechanism of RGO-Fe_3O_4 composites. *RSC Adv.* **2013**, *3*, 23638−23648.

(58) Moitra, D.; Ghosh, B.; Chandel, M.; Jani, R.; Patra, M.; Vadera, S.; Ghosh, N. Synthesis of a $Ni_{0.8}Zn_{0.2}Fe_2O_4$-RGO nanocomposite: an excellent magnetically separable catalyst for dye degradation and microwave absorber. *RSC Adv.* **2016**, *6*, 14090−14096.

(59) Naito, Y.; Suetake, K. Application of ferrite to electromagnetic wave absorber and its characteristics. *IEEE Trans. Microwave Theory Tech.* **1971**, *19*, 65−72.

(60) Zhang, M.; Jiang, Z.; Lv, X.; Zhang, X.; Zhang, Y.; Zhang, J.; Zhang, L.; Gong, C. Microwave absorption performance of reduced

graphene oxide with negative imaginary permeability. *J. Phys. D: Appl. Phys.* **2019**, *53*, No. 02LT01.

(61) Lu, Z.; Wang, Y.; Di, X.; Cheng, R.; Yang, L.; Gao, P. Design of hierarchical core-shell $ZnFe_2O_4@MnO_2@RGO$ composite with heterogeneous interfaces for enhanced microwave absorption. *Ceram. Int.* **2022**, *48*, 5217−5228.

(62) Wang, Y.; Di, X.; Chen, J.; She, L.; Pan, H.; Zhao, B.; Che, R. Multi-dimensional C@ NiCo-LDHs@Ni aerogel: Structural and componential engineering towards efficient microwave absorption, anti-corrosion and thermal-insulation. *Carbon* **2022**, *191*, 625−635.

(63) Cheng, R.; Wang, Y.; Di, X.; Lu, Z.; Wang, P.; Ma, M.; Ye, J. Construction of MOF-derived plum-like NiCo@C composite with enhanced multi-polarization for high-efficiency microwave absorption. *J. Colloid Interface Sci.* **2022**, *609*, 224−234.

(64) Cheng, R.; Wang, Y.; Di, X.; Lu, Z.; Wang, P.; Wu, X. Heterostructure design of MOFs derived $Co_9S_8/FeCoS_2/C$ composite with efficient microwave absorption and waterproof functions. *J. Mater. Sci. Technol.* **2022**, *129*, 15−26.